

The Influence of the Bulk Reduction State on the Surface Structure and Morphology of Rutile TiO₂(110) Single Crystals

Min Li, Wilhelm Hebenstreit, and Ulrike Diebold*

Department of Physics, Tulane University, New Orleans, Louisiana 70118

Alexei M. Tyryshkin, Michael K. Bowman, Glen G. Dunham, and Michael A. Henderson

Pacific Northwest National Laboratory, Richland, Washington 99352

Received: December 9, 1999; In Final Form: March 6, 2000

We have investigated the relationship between different types and amounts of bulk defects and the surface morphology of TiO₂(110) single crystals prepared by annealing in ultrahigh vacuum and in oxygen. Rutile TiO₂(110) specimens were cut from the same crystal and were heated in a furnace to different temperatures which resulted in different states of reduction (colors of the crystals). After characterization of the bulk defects with electron paramagnetic resonance (EPR), the specimens were studied with scanning tunneling microscopy (STM), low-energy He⁺ ion scattering (LEIS), and work function measurements. EPR reveals that darker rutile crystals exhibit higher concentrations of extended Ti³⁺ related bulk defects such as crystallographic shear planes (CSP), with a decrease in substitutional and interstitial defects as compared to lighter crystals. Surface structures with (1 × 2) features are preferably formed upon UHV annealing on these darker crystals. LEIS measurements show that all of the crystals' (110) surfaces are reoxidized upon annealing in ¹⁸O₂ (573 K, 1 × 10^{−6} mbar, 10 min) and that the ¹⁸O surface content is proportional to the bulk reduction state. UV–visible adsorption spectra and resistivity measurements also scale with the reduction states of crystals. Only the (1 × 1) structure is observed on the surface of slightly reduced crystals. Annealing in oxygen induces additional metastable structures, i.e., TiO₂ clusters on blue crystals and rosette networks on dark blue crystals.

1 Introduction

TiO₂ finds wide applications as photocatalyst, gas sensor, and catalyst.^{1–3} In addition, the TiO₂(110) surface has received intensive attention as a prototype for metal oxide surfaces. Many STM (scanning tunneling microscopy) studies on the structure and morphology of the (110) surface have been reported. There is general agreement that two phases, (1 × 1) and (1 × 2), exist in different temperature ranges after UHV or oxygen annealing.^{4–15} The presence of bulk defects (e.g., oxygen vacancies, Ti³⁺ interstitials, crystallographic shear planes (CSP)) plays an important role in the creation of different phases on the surface, for example, Ti³⁺ in the Ti₂O₃ model of the (1 × 2) structure¹⁰ and CSP for the step edge orientation on heavily reduced (110) surfaces.^{16–18} Recently, Bennett et al.⁴ found that two different (1 × 2) phases form during oxygen annealing, depending on the reduction states of samples. A stable Ti₂O₃ type structure is formed on “medium blue” crystals and a highly reactive, cross-linked (1 × 2) structure on “dark blue/black” crystals. This cross-linked (1 × 2) structure is an intermediate state for the growth of (1 × 1) islands in the reoxidation process. Recently, our group reported an additional phase consisting of rosette networks, short (1 × 2) of the Ti₂O₃-type strands, and added small (1 × 1) islands which are induced by annealing flat TiO₂(110) surfaces in oxygen at moderate temperatures.^{19–22} These structures are produced in a reoxidation process in which excess Ti migrates from the reduced bulk to the surface and reacts with gaseous oxygen to form additional TiO₂ layers. In

our previous work,^{21,22} we found indications that the formation of oxygen-induced features is influenced by the reduction state of TiO₂ samples in addition to several other factors such as annealing temperature, annealing time, and oxygen pressure. So far, no attempt has been made to relate surface morphology to a quantitative study of bulk defects in rutile crystals.

In this paper, the types and amounts of defects of different rutile crystals are quantified with EPR measurements prior to surface science investigations. The surface morphology after UHV and oxygen annealing is studied using a combination of STM, low-energy He⁺ ion scattering (LEIS), and work-function measurements. Mounting several crystals on one sample platen and treating them simultaneously ensures the same oxidation conditions. We find crystal color dependent surface morphologies that are rationalized with rate-dependent growth of additional TiO₂. These results give guidance on how to prepare either a stoichiometric TiO₂(110) (1 × 1) surface or one covered with a metastable rosette structure for various surface chemistry studies.

2 Experimental Section

The experiments were carried out in a commercial OMI-CRON UHV system equipped with XPS (X-ray photoelectron spectroscopy), LEIS (low-energy He⁺ ion scattering spectroscopy), LEED (low-energy electron diffraction), and STM (scanning tunneling microscopy).^{20,23} STM measurements were performed in constant-current mode at room temperature with positive sample bias voltages of less than 2.0 V. The roughness of surfaces is quantified with the root-mean-square (RMS) value,

* Corresponding author. Fax: (504) 862-8702. E-mail: diebold@mailhost.tcs.tulane.edu.

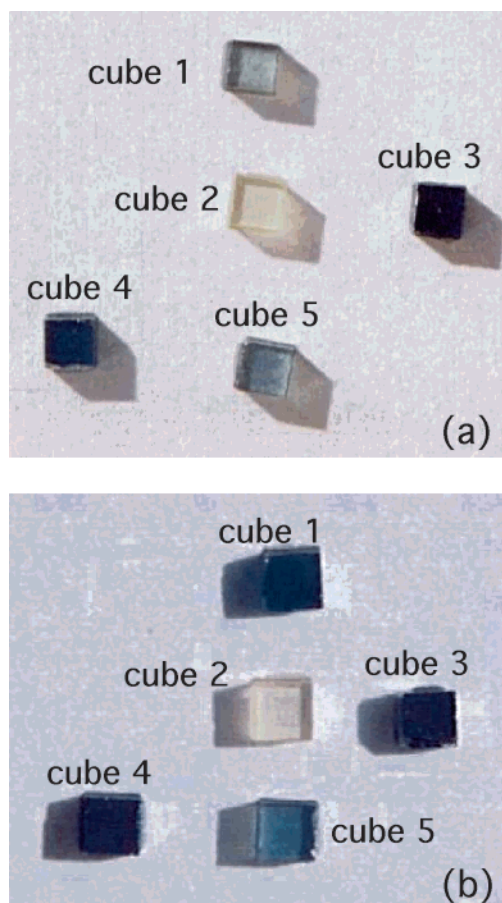


Figure 1. Photographs of rutile crystals taken (a) before insertion into the UHV chamber and (b) after extended experiments on cubes 1, 3, and 4. See Table 1 for reduction conditions.

which is determined on the differentiated STM images. The RMS values quoted in the results section have been obtained by taking the average of several images of the same surface. The maximum error of the RMS measurements is 0.08 Å. For oxygen exposure experiments, $^{18}\text{O}_2$ gas ($^{18}\text{O}_2$: $^{16}\text{O}_2$ = 93%:7%) was used. Gas dosing was performed by backfilling the chamber. In LEIS spectra, ^{18}O and ^{16}O peaks are clearly separable,²¹ and the surface content of ^{18}O and ^{16}O was quantified with Gaussian peak fitting after subtraction of a linear background. Relative changes in sample work functions were measured by monitoring the low-energy cutoff of the secondary electron spectrum excited by a focused He^+ beam ($E = 1225$ eV, $p = 1.2 \times 10^{-8}$ mbar) with a bias voltage of -8 V applied to the sample.

A large polished single rutile crystal (Commercial Crystal Growers) was cut into nine small cubes (~ 2 mm \times 2 mm \times 2 mm) using a diamond saw. Each crystal cube was heated separately in a furnace, which gave rise to the color change depicted in Figure 1a. The heating temperature and time is given in Table 1. The crystal color is correlated with heating temperature rather than time. Before reduction, all cubes were transparent, similar to cube 2 (which was reoxidized in air from a color similar to cube 3, Table 1).

For EPR measurements, the sample cubes were placed in a fused silica EPR tube (707-SQ-250M from Wilmad). One of the crystallographic axes ([110] or [001]), which coincided with one of the edges of the cube, was held along the tube axis with a small wooden stick. The tube was mounted in a single-axis goniometer (ER218 PG1, Bruker Instruments) and EPR spectra were taken every five degrees as the sample was rotated. The EPR spectra did not change unexpectedly with temperature over

the range 10–40 K, although some lines in the spectrum did broaden or become easily saturated in this range. Most of the EPR lines were sharp with line widths of 10–20 mT. Spectra were recorded on a Bruker ESP-380e spectrometer using an X-band rectangular resonator (ER4102ST, Bruker) mounted on a helium cryostat (ER4112 HV, Bruker).

Over twenty different paramagnetic species were found in the set of crystals in the spectral region between 320–400 mT. Where possible, their spectra were followed in both planes of the crystal rotations and each species classified in two ways. A Ti(III) species will have a single strong line from the 87.2% of Ti(III) that has an even isotopic weight and a nuclear spin of zero. The other 12.8% of the intensity from 47,49 Ti(III) is split into eight lines, with the hyperfine interaction of 0.5–3.0 mT. Where such a pattern of an intense central line flanked by eight weak hyperfine split lines could be observed, that species was classed as a Ti species. All others were classed as non-Ti. The quantity of each species was estimated in each sample by integration of the major line and corrected, for Ti(III), by the calculated amount in the hyperfine lines. The other method of classifying species was based on the symmetry of the patterns of EPR spectra in the crystal rotations. The symmetry of the electron distribution around a nucleus is determined by the symmetry of the crystal field at the nucleus and consequently is reflected in the anisotropies in the g and hyperfine matrices characteristic of each species. In brief, for either a substitutional or the usual interstitial site, one of the principle directions of both the g and hyperfine matrices must be observed for the magnetic field applied along the [001] axis of the crystal. Otherwise, the site has lower symmetry, either because the defect is at neither of those locations or the local crystal symmetry has been lost. Similarly, the other principal values of these matrixes must occur along the [110] and $[\bar{1}\bar{1}0]$ directions for the substitutional, but not the interstitial site. Thus, species are classified as substitutional, interstitial, or no symmetry.

EPR images were made of the distribution of several major species in the cubes. A linear field gradient was applied along the direction of the field from the EPR magnet. EPR spectra of one species were recorded as the sample was rotated in the gradient. Fourier deconvolution of spectra with and without a gradient was used to recover the projections needed to reconstruct the image using standard, filtered back-projection methods.

For the surface experiments, three cubes (cube 1, 3, and 4) were mounted side-by-side on one Ta sample platen to ensure the same sample preparation conditions. Two cubes (2 and 5) were mounted together on a separate platen. The samples were fixed using strips of Ti foil (thickness: 0.127 mm) to avoid sputtering of foreign elements onto the crystals. All five cubes showed initial Ca segregation.²³ After several cycles of UHV sputtering and annealing, no impurities were detected in LEIS spectra.

During the course of these experiments, the color of the crystals changed. After sputtering and annealing in UHV (total ~ 690 min at 973 K), the light-blue sample (cube 1) changed to a color similar to cube 4 (see Figure 1b), while the colors of the two heavily reduced samples (cubes 4 and 3) became darker compared to Figure 1a and were no longer differentiable from each other. This indicates that the near-stoichiometric rutile crystals can be reduced easily until they turn to a color specific to the highest annealing temperature.

After these experiments, the light adsorption of the crystals was characterized using a UV–visible spectrophotometer (Cary

TABLE 1: Sample Reduction Conditions for the Samples Shown Figure 1

	cube 2	cube 5	cube 1	cube 4	cube 3
before insertion into UHV (Figure 1a)	21 h 40 min at 1450 K	1 h 10 min at 1350 K	19 h at 1273 K	35 min at 1450 K	4 h 55 min at 1450 K
after extended experiments on cubes 1, 3, and 4 (Figure 1b)	(as cube 3) then reoxidized at 1450 K				after daily sputtering and UHV annealing for a total time of 690 min at 973 K

TABLE 2: Concentration of Bulk Defects from EPR (arb. units)

defect type	cube 1 (light blue)	cube 5 (light blue)	cube 4 (blue)	cube 3 (dark blue)
Ti _{substitutional}	116	190	255	588
Ti _{interstitial}	125	206	6.24	1.24
Ti _{no symmetry}			472	378
non-Ti _{substitutional}	197	558		
non-Ti _{interstitial}			148	173
non-Ti _{no symmetry}			1080	731
STM results (UHV anneal)	no (1 × 2) strands	no (1 × 2) strands	(1 × 2) strands	(1 × 2) strands
STM results (oxygen anneal)	similar to UHV anneal	similar to UHV anneal	TiO ₂ clusters	rosette networks

100 Scan, Varian). Two similar aluminum plates (thickness: ~0.90 mm) with a small hole (<2 mm in diameter) were made specifically for both the crystals and the reference beam and were fixed in standard Varian sample holders. One of these holders was for the reference beam, and the second one to mount the crystals. The resistivity was measured using a PPMS (physical property measurement system, Quantum Design, model 6000). In the PPMS experiments, two thin copper–lead wires (~50 μ m in diameter) were attached to both sides (perpendicular to the [110] direction) of each cube (the sides were coated with silver glue). Electrical current was supplied in the direction perpendicular to the [110] direction. The resistance was measured after the sample had been kept at 300 K for 30 min.

3 Results

3.1 EPR Measurements of Bulk Defects. Table 2 shows the concentration of bulk defects of cubes 5, 1, 4, and 3 from EPR measurements. The designations “non-Ti” refer to spins that are not Ti related (e.g., Fe³⁺, ²⁴). The Ti_{no symmetry} features are most likely extended defects such as crystallographic shear planes or platelets.²⁵ Features labeled as Ti_{substitutional} are Ti³⁺ states associated with oxygen vacancies. Accordingly, non-Ti_{substitutional} correlates with impurity-related oxygen vacancies. For example, with Cr³⁺ replacing Ti⁴⁺ as a substitutional in TiO₂, an oxygen vacancy at a neighboring site might be created.²⁶ Note that the concentration of Ti_{interstitial} goes down dramatically from cube 5 to 3, with the appearance of extended defects Ti_{no symmetry}. Compared to cube 1, there is a slight increase of Ti_{substitutional} and Ti_{interstitial} in cube 5. Cubes 4 and 3 are generally quite similar to each other except for the obvious increase of Ti_{substitutional} and decrease of Ti_{interstitial} in cube 3. It is interesting that non-Ti_{substitutional} exists only in the slightly reduced samples (cube 5 and 1), while non-Ti_{interstitial} and non-Ti_{no symmetry} appear only in heavily reduced samples (cubes 4 and 3). EPR mapping showed that the defect concentration was fairly uniform throughout the bulk, with the exception of one defect in cube 6 which was strongly localized and may be a contaminated spot in that cube. Diffusion at these temperatures is high enough to ensure an even distribution of features with unpaired spins, even though they are produced through a loss of oxygen on the surface. No features with unpaired spins have been observed in the EPR measurements of cube 7 (unreduced, not shown in Figure 1) or cube 2 (reduced as cube 3 and then reoxidized to the transparent state, Table 1, Figure 1).

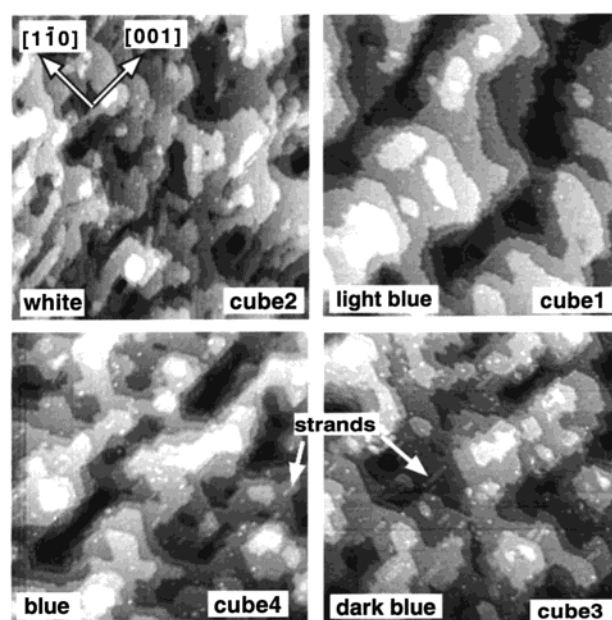


Figure 2. STM images (1000 Å × 1000 Å) of four TiO₂(110) crystals with different bulk reduction states prepared by sputtering and UHV annealing at 973 K for 20 min.

3.2 UHV Annealing of TiO₂(110) Surfaces. Figure 2 shows STM results of TiO₂(110) surfaces for four cubes prepared by sputtering and UHV annealing for 20 min at 973 K. The morphology of the light-blue cube 5 is similar to that of cube 1 and is not presented here. The reoxidized cube 2 was reduced at 973 K for 60 min in UHV to make it conductive for the STM measurement, which changed its color to transparent with a light-blue hue. The STM images presented here were taken after daily sputtering and UHV annealing at 973 K for ~200 min (cube 2) and ~300 min (cubes 4, 1, and 3). There is a pronounced difference in the surface roughness. The two darker samples (cubes 4 and 3) and cube 2 are somewhat “rougher” with narrow terraces and more (1 × 1) islands (typical size of 50 Å × 70 Å). From RMS analysis, the two darker crystals and the reoxidized one have higher RMS values (blue cube 4: RMS = 1.14 Å; dark-blue cube 3: RMS = 1.25 Å; cube 2: RMS = 1.07 Å) compared to the RMS value of 0.98 Å for the light-blue cube 1. Notice also that both cubes 4 and 3 exhibit several bright rows (typically 40 Å long) along the [001] direction which are not observable on cubes 2 and 1. These rows are commonly named (1 × 2) strands. In a recent paper¹⁹

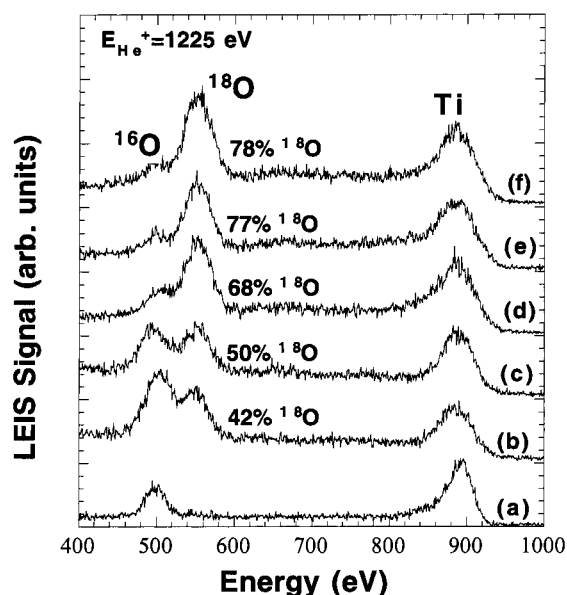


Figure 3. LEIS spectra of TiO₂(110) surfaces prepared by (a) sputtering and UHV annealing for 20 min at 773 K and after subsequent reannealing the UHV annealed surface in ¹⁸O₂ (1×10^{-6} mbar) for 10 min at 573 K for (b) cube 2 (white); (c) cube 5; (d) cube 1; (e) cube 4; and (f) cube 3.

we show that they consist of Ti₂O₃ as originally suggested by Onishi et al.⁹ The step edges of terraces on the two darker samples and the reoxidized cube 2 are more regular than those on the light-blue sample (cube 1). Normally, they are oriented in the $\langle 001 \rangle$ and $\langle 111 \rangle$ directions.²⁷ The deep “holes” on the four surfaces result possibly from sputter damage that is not recovered completely during the UHV anneal. The heavily reduced sample (dark-blue cube 3) exhibits a slightly higher work function of 0.2 eV than the lighter samples. The work function is very sensitive to the state of the surface, albeit in an unspecific way. It can change significantly upon the addition and removal of surface adatoms or a change of surface defect density. For *n*-type metal oxides, the removal of surface oxygen (occurring probably via desorption of molecular O₂ at high temperatures, which leaves behind extra electrons in the resulting vacancies) results in an accumulation layer, i.e., a surface region where carrier concentration is higher than in the bulk.¹ A surface double layer with the negative pole directed outward is produced which increases the work function. Therefore, the measured relatively higher work function on the dark-blue cube 3 might be an indication of more oxygen vacancies on the surface of the heavily reduced sample.

3.3 Oxygen Annealing of TiO₂(110) Surfaces. Figure 3 shows LEIS spectra of the five TiO₂(110) samples, reannealed in ¹⁸O₂ (1×10^{-6} mbar) for 10 min at 573 K. The reference spectra from the UHV-annealed surface was similar for all the samples. The one shown in Figure 3a was obtained from cube 3. The incorporation of ¹⁸O is substantial in all cases. The LEIS measurements were performed after prolonged annealing of in-vacuum treatment by sputtering/annealing cycles of cubes 4, 1, and 3, which led to a crystal color similar to Figure 1b. Note that LEIS is an extremely surface-sensitive technique that gives information about the topmost surface layer only. Many layers of additional TiO₂ are formed before ¹⁸O saturates on the surface.²¹ This is also reflected in the difficult removal of ¹⁸O from reoxidized surfaces. For example, after several cycles of sputtering (total sputter time 240 min with 2000 eV Ar⁺ beam, $I_{\text{sample}} = 1 \mu\text{A}$), a trace of ¹⁸O is still visible in LEIS spectra.

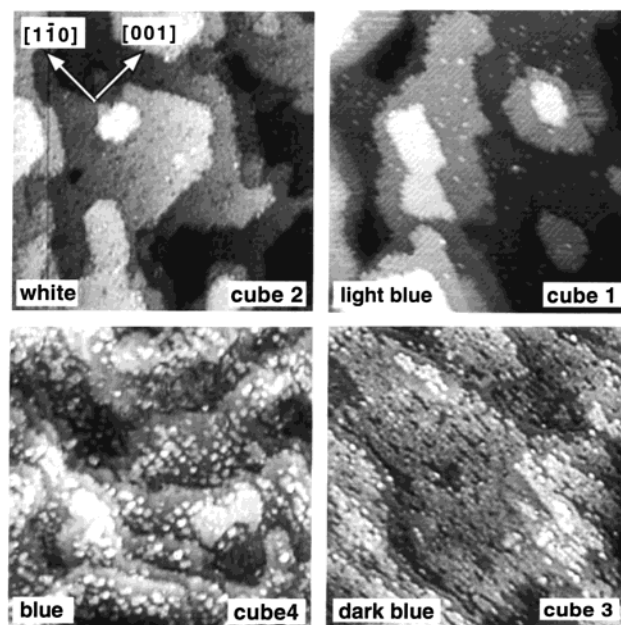


Figure 4. STM images ($500 \text{ \AA} \times 500 \text{ \AA}$) of four TiO₂(110) crystals prepared by annealing in ¹⁸O₂ (1×10^{-6} mbar) the UHV annealed surfaces in Figure 2 for 10 min at 573 K.

Figure 4 shows STM images ($500 \text{ \AA} \times 500 \text{ \AA}$) of the four TiO₂(110) surfaces prepared similar to those for LEIS measurements. The history of STM images presented here is similar to that of Figure 1b. It is noticeable that cubes 2 (reoxidized) and 1 (light blue) do not exhibit any rosettes, despite being heavily enriched with ¹⁸O (Figure 3). The surface morphology is remarkably similar to the UHV annealed surfaces (Figure 2). The small bright features scattered across the terraces on cube 1 are probably due to some sort of contamination. (Such features are also present on the UHV annealed surface. Their concentration is below the detection limit of LEIS, hence we cannot assign their origin.) On cube 4 (blue cube) a large amount of white clusters is evenly distributed across the substrate. The appearance of this sample is reminiscent of darker TiO₂ crystals that have been annealed to lower temperatures in our previous work.²¹ (The TiO₂ crystal used previously in the experiments of reference 17 appears dark blue.) We can exclude any kind of contamination as being the main cause for these clusters; any element with such a high coverage should clearly be observable in XPS and LEIS. Cube 3 (dark blue) is completely covered with rosette networks and (1×1) islands. The step edges of (1×1) terraces of both cubes 4 and 3 are irregular. A small-scale STM image ($300 \text{ \AA} \times 300 \text{ \AA}$) (Figure 5) reveals the rosette network (“R”) and (1×1) islands which were reported previously.^{20–22} LEED for such restructured surfaces shows a (1×1) pattern with an increased background.

Annealing in oxygen increases the work function of each sample by 0.7 eV. The darkest sample (cube 3) has again a somewhat higher work function (~ 0.2 eV) than all of the other samples. If the surfaces are covered with adsorbed oxygen, a depletion layer might occur due to the charge transfer from surfaces to adsorbed oxygen.¹ Again, this gives rise to a surface dipole layer with its negative pole (O²⁻) outward, and the work function of the electrons in the surface increases²⁸ in agreement with our work function measurements. UHV annealing dark samples leads to a higher work function which indicates a higher charge density (or O vacancy density) on surfaces. Possibly, this might result in a relatively strong charge transfer from surfaces to adsorbed oxygen and further contribute to the surface

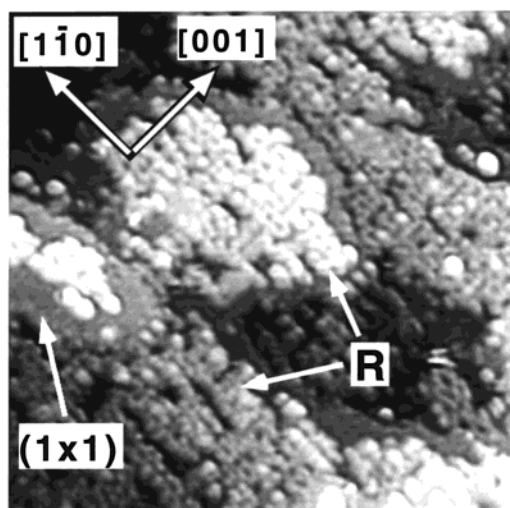


Figure 5. A small-scale STM image ($300 \text{ \AA} \times 300 \text{ \AA}$) of cube 3 in Figure 4.

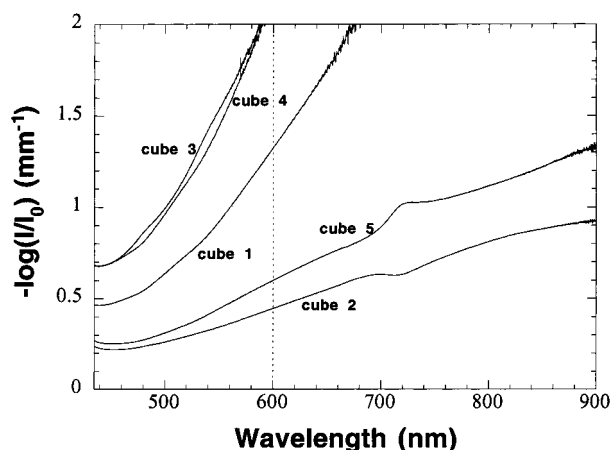


Figure 6. UV-visible adsorption spectra of five rutile crystals with different reduction states.

dipole layer which is indicated by a 0.2 eV higher work function on the dark-blue cube in our measurements.

Several surface morphology studies involving CSP step edges have been reported.^{16–18,29} Step edges with half of the height of normal TiO_2 (110) step edges are oriented along several specific directions (i.e., $\{132\}$ series, $[1\bar{1}0]$, $[1\bar{1}1]$ and $[1\bar{1}3]$), which were assigned as the interception of bulk CSP with (110) plane in these previous studies. However, no CSP-related step edges are found on the surfaces of our crystals (Figure 2, cubes 4 and 3). Probably the samples are not reduced enough for observable nucleation of CSP on the surface.

3.4 UV-Visible Adsorption Measurements of Crystals.

The adsorption spectra of five cubes in the visible light region are shown in Figure 6. The measured absorbance was divided by the path length of 2 mm (the thickness of crystals). For the darker crystals (cubes 4 and 3), the adsorption above 600 nm was beyond the detection limit of the instrument due to the thickness of crystals. The adsorption curves of cube 1, 5, and 2 above 600 nm scales with their crystal colors as illustrated in Figure 1b. The assignment of optic transitions is related to the excitations within various types of defect levels.²⁶ For alkali halide crystals, the broadened peaks in the adsorption spectrum are associated with the various combinations of F-centers.³⁰ Possibly, the resonant excitation of electrons from energy levels of both oxygen vacancies (F-center¹) and Ti interstitials might contribute to the observed adsorption spectra.

TABLE 3: Sample Resistivity ($\Omega\cdot\text{cm}$)

	cube 2	cube 5	cube 1	cube 4	cube 3
resistivity	1835.0	108.24	46.76	24.06	8.94

3.5 Resistivity Measurements of Crystals. Table 3 shows the resistivity of the five cubes from PPMS measurements at 300 K. The lighter crystals have a higher resistivity than the darker crystals. This is in agreement with the results from a early transport study of *n*-type rutile in the temperature region of 2–600 K³¹ in which the heavily compensated *n*-type rutile (which means slightly reduced samples in our experiments) has a high resistivity than the slightly compensated sample. In this paper, it was proposed that either oxygen vacancies (F-centers) or Ti interstitials might be the donors for the electrons excited to the conduction band. Acket et al.³² concluded that the donors in reduced rutiles are probably Ti interstitials. Accordingly, the resistivity of rutile crystals correlates with the defects in the bulk and assists in the characterization of the reduction level of rutile crystals.

4 Discussion

The main experimental results for annealing in UHV and oxygen are summarized in the lower part of Table 2. The surface preparation results of cube 2 (not listed in Table 2) are similar to cubes 1 and 5. Originally, cube 2 showed none of the EPR features listed in Table 2, but it was slightly reduced before the STM measurements. This led to a light-blue color, similar to cubes 1 and 5 in Figure 1a, and, conceivably, to similar bulk defect properties. For all samples we observe a clear correlation between the number and type of defects observed in EPR and the main surface features seen with STM. The occurrence of features other than the regular, (1×1) terminated terraces correlates with (1) the onset of extended defects such as CSPs of intrinsic (Ti_{no} symmetry) as well as extrinsic nature (non- Ti_{no} symmetry), concurrent with (2) a drastic decrease (by 2 orders of magnitude) of interstitial Ti atoms; (3) a gradual increase in the concentration of bulk oxygen vacancies ($\text{Ti}_{\text{substitutional}}$); and (4) a dramatic alteration in the character of non-Ti related defects (onset of non-Ti related interstitial atoms and disappearance of non- $\text{Ti}_{\text{substitutional}}$).

Before analyzing these results in more detail, a note of caution is in order. First, bulk defect species which are detected during EPR analysis at 10–40 K are those present in the cube at room temperature after it was rapidly cooled at the end of the high-temperature treatment and may be different from those present at high temperatures. Crystallographic shear planes oriented along $[132]$ and $[143]$ directions were reported in rutile reduced at 1323 K after slow cooling to room temperature.^{25,33} However, only small platelet and cluster defects are formed upon rapid cooling, suggesting that a kinetically limited precipitation process is involved in CSP formation.²⁵ Since there is no direct evidence that these extended defects are present at high temperatures, one could assume that at high temperature all of the bulk defects in rutile are point defect in nature, with precipitation/agglomeration occurring only upon cooling. Second, the crystal color changes induced by sputtering and UHV annealing, as exemplified in Figure 1b, have to be kept in mind. The concentration of Ti interstitials/substitutionals in the bulk probably increased during the course of our experiment. UHV annealing would only decrease the bulk Ti interstitials by precipitation into extended defects such as CSPs, while sputtering followed by UHV annealing above 700 K could possibly produce more Ti^{3+} interstitials in the bulk.³⁴ Nevertheless, the clear correlation observed in Table 2 makes us confident to use

the EPR results as a guideline for interpretation of reduction state related surface morphology. As we will show in the following, enhanced diffusion of excess Ti to the sample surface probably accounts for all of the observed differences.

Reoxidation takes place on all five samples upon high-temperature annealing in oxygen, but the incorporation of ¹⁸O takes place at smaller rates on more stoichiometric crystals as compared with more reduced ones (Figures 1b and 3). The growth mode of additional TiO₂ is strikingly different on the five samples. A clear clustering is observable on cube 4 (blue) and cube 3 (dark blue), and both samples exhibit metastable structures in addition to (1 × 1) islands. The surface of cube 3 (dark-blue/black) (Figures 4 and 5) closely resembles oxygen-induced features that are discussed in refs 20–22. These features are absent on cubes 1 and 5, as well as on the reoxidized cube 2 (Figure 4). The (1 × 1) structure is formed exclusively on these more stoichiometric samples. The surfaces look no different than after UHV annealing, which indicates that additional TiO₂ grows in a two-dimensional (2D) or step-flow mode.

This growth behavior can probably be attributed to a very different arrival rate of Ti on the sample surface, which in turn should be related to the types and/or concentrations of bulk defects. Step-flow mode growth is known to occur under conditions with very small growth rates (i.e., deposition rates³⁵) in homoepitaxial systems. Adatoms with high mobility diffuse to residual steps, causing the steps to simply propagate across the surface.³⁶ The step edges may act as a sink for the adatoms on the lower terrace in the 2D growth mode.³⁵ Nucleation on terraces (3D growth mode) may typically occur under conditions where the growth rate is higher. At slow growth rates, the additional TiO₂ on the surface has time to relax into the (1 × 1) structure by diffusing and incorporating into the (1 × 1) step edges, and no metastable rosette networks are formed by nucleation.

The TiO₂ growth rate can be varied by either adjusting the oxygen pressure or by changing the arrival rate of Ti from the bulk during oxidation of TiO₂. A change in the oxygen pressure indeed influences the growth mode.³⁷ On a relatively dark crystal, only (1 × 1) islands and (1 × 2) strands are observed after an exposure to 1 × 10^{−7} mbar oxygen at a temperature of 670 K. When the pressure is increased to 1 × 10^{−6} mbar the usual rosette networks are observed.³⁷ In this work, the very different arrival rate of Ti to the sample surface must be related to the amount and/or mobility of excess Ti in the bulk.

Interstitial Ti atoms are very mobile through diffusion along open channels in the <001> and <110> directions in rutile crystals,³⁸ and one would assume that a high concentration of Ti_{interstitial} would correlate with 3D nucleation on the surface. Yet, the concentration of interstitial Ti atoms decreases with a higher bulk reduction state. Nucleation and formation of metastable structures are correlated with the presence of extended defects (Ti_{no symmetry}, Table 2). Bursill et al.²⁵ pointed out that the precipitation phenomenon of extended defects is very strongly temperature dependent. For precipitation and dissolution of platelets, higher temperatures are required. Accordingly, these extended defects are unstable at higher temperatures, and excess Ti is released which migrates in an interstitial diffusion mechanism to the surface. It has been shown³⁹ that impurities in rutile crystals affect diffusion rates. While different impurity concentrations can clearly be excluded (all five samples have been cut from the same crystal), the cubes do exhibit very different configurations according to the EPR measurements (Table 2) (EPR detects impurities only with spin

states. In all likelihood, the bulk concentration of the various impurities is the same in all of the cubes, and only the concentration of detectable spin states is being changed by reduction.) Maybe this contributes to the observed differences in Ti_{interstitial} diffusion rates as well. The diffusion of oxygen vacancies occurs at a much smaller rate as compared to Ti interstitial.^{40–42} The gradual increase of the concentration of Ti_{substitutional} probably plays a minor role in the observed differences in surface morphology.

Sputtering and UHV annealing is the most popular method by which to prepare flat, almost stoichiometric (1 × 1) surfaces. Sputtering preferentially removes oxygen from the surface, and “bulk-assisted reoxidation” restores the surface stoichiometry at elevated temperatures. Henderson has shown that excess Ti³⁺ from sputtered surfaces diffuses into bulk above 700 K,³⁴ which reduces the crystals further. For annealing below 1000 K, various groups have reported scattered (1 × 2) strands on (1 × 1) terminated surfaces,^{5–7,12,22,43} while these are absent in other investigations.^{8,9,27,44} As our results show, the level of bulk reduction is an important parameter for the formation of (1 × 2) structures under UHV conditions. Most likely, the observed (1 × 2) strands exhibit a Ti₂O₃ stoichiometry.^{4,8,19} As discussed above, the diffusion of Ti interstitials in the more reduced crystals (cubes 3 and 4) is much higher than in the three lighter crystals, because of a higher bulk Ti content precipitated as extended defects and/or because of the different geometry of non-Ti related defects. When the surfaces are exposed to oxygen, excess Ti arriving at the surface reacts to TiO₂. The surface acts as a sink for interstitial Ti, and a gradient in chemical potential is established that drives Ti out of the bulk. When annealing in UHV, there is an equilibrium between diffusion of excess Ti into and out of the bulk, and a higher bulk concentration necessitates a higher concentration of surface Ti. This shift of the dynamic equilibrium toward more Ti interstitials in the near-surface region may contribute to the formation of reduced Ti₂O₃ strands.

Interestingly, annealing in oxygen produces similar strands on TiO₂ surfaces for certain degrees of bulk reduction. Without a quantitative measure of sample reduction state and/or color, reports by different authors are hard to compare, but annealing in oxygen induces similar features on “deep-blue”¹⁰ and “medium-blue”⁴ crystals, whereas “dark-blue/black” crystals⁴ oxidize through cross-linked (1 × 2) strands that are precursors to the regular (1 × 1) structure.

5 Summary

The color (reduction state) of rutile crystals plays an important role in the preparation of TiO₂(110) surfaces. The bulk defects of five samples with varying degrees of bulk reduction have been characterized with EPR. The crystals can be grouped in two subsets that show distinctly different EPR signatures and surface morphologies after preparation through annealing in either oxygen or UHV.

More stoichiometric samples showed no signs of extended defects (such as CSPs) in the bulk as identified by unpaired spins on either Ti or impurity atoms before the surface science experiments. Annealing in UHV as well as in ¹⁸O₂ renders (1 × 1) terminated surfaces. Enrichment in the near-surface region with isotopically labeled ¹⁸O shows substantial regrowth of additional TiO₂(110)(1 × 1) in a step-flow mode. The surface content of ¹⁸O scales with the bulk reduction state.

More reduced crystals are characterized by a marked decrease in the content of interstitial Ti and the presence of extended defects in the bulk. The surfaces of these crystals show (1 × 2)

features, interpreted as added Ti_2O_3 rows after UHV annealing. The surfaces exhibit added clusters and metastable rosette networks induced by reoxidation. Neither CSPs extending to the surface nor cross-linked (1×2) rows were observed.

These variations in surface morphologies are attributed to differences in the arrival rate of excess Ti at the surface, which depends on the amount and/or mobility of excess Ti in the bulk.

Guidelines of surface preparation of $\text{TiO}_2(110)$ can be extracted from this work. If solely (1×1) terminated surfaces are desired, light-blue crystals (as depicted in Figure 1) should be used. Annealing in oxygen will then result in stoichiometric, (1×1) terminated surfaces. On the other hand, more complex morphologies with a range of different coordination sites (Figure 5) can be formed if dark crystals are annealed in oxygen. Such a rich array of surface structures may provide a playground for surface science experiments where the influence of different adsorption sites can be tested. The color pictures, resistivity and UV-vis adsorption data presented in this work can be used as a semiquantitative measure for preparing a TiO_2 crystal with the desired stoichiometry, hence surface properties.

Acknowledgment. This work was supported in part by NSF-CAREER and DoE-EPSCoR (Tulane). The EPR work was supported by the U.S. Department of Energy, Environmental Management Science Program, and was conducted at the William R. Wiley Environmental Molecular Science Laboratory, a Department of Energy user facility funded by the Office of Biological and Environmental Research. Pacific Northwest National Laboratory is a multiprogram national laboratory operated for the U.S. Department of Energy by Battelle Memorial Institute under contract DE-AC06-76RLO 1830. The authors thank Professor Russell H. Schmehl for his support with the UV-visible adsorption measurements and Professor Srikanth Hariharan and Dr. Leonard Spinu for their help with the resistivity measurements.

References and Notes

- (1) Henrich, V. E.; Cox, P. A. *The Surface Science of Metal Oxides*; Cambridge University Press: Cambridge, 1994.
- (2) Wang, R.; Hashimoto, K.; Fujishima, A.; Chikuni, M.; Kojima, E.; Kitamura, A.; Shimohigoshi, M.; Watanabe, T. *Nature* **1997**, *388*, 431.
- (3) *Sensors—A Comprehensive Survey*; Göpel, W.; Hesse, J.; Zeinel, J. N., Eds.; VCH: Weinheim, 1991.
- (4) Bennett, R. A.; Stone, P.; Price, N. J.; Bowker, M. *Phys. Rev. Lett.* **1999**, *82*, 3831–3834.
- (5) Berkó, A.; Solymosi, F. *Langmuir* **1996**, *12*, 1257–1261.
- (6) Murray, P. W.; Condon, N. G.; Thornton, G. *Phys. Rev. B* **1995**, *51*, 10989.
- (7) Novak, D.; Garfunkel, E.; Gustafsson, T. *Phys. Rev. B* **1994**, *50*, 5000.
- (8) Onishi, H.; Iwasawa, Y. *Surf. Sci. Lett.* **1996**, *313*, 783–789.
- (9) Onishi, H.; Fukui, K.; Iwasawa, Y. *Bull. Chem. Soc. Jpn.* **1995**, *68*, 2447–2458.

- (10) Onishi, H.; Iwasawa, Y. *Phys. Rev. Lett.* **1996**, *76*, 791–794.
- (11) Pang, C. L.; Haycock, S. A.; Raza, H.; Murray, P. W.; Thornton, G. *Phys. Rev. B* **1998**, *58*, 1586–1589.
- (12) Sander, M.; Engel, T. *Surf. Sci. Lett.* **1994**, *302*, 263.
- (13) Szabo, A.; Engel, T. *Surf. Sci.* **1995**, *329*, 241–254.
- (14) Tanner, R. E.; Castell, M. R.; Briggs, G. A. D. *Surf. Sci.* **1998**, *412/413*, 672–681.
- (15) Xu, C.; Lai, X.; Zajac, G. W.; Goodman, D. W. *Phys. Rev. B* **1997**, *56*, 13464.
- (16) Rohrer, G. S.; Henrich, V. E.; Bonnell, D. A. *Surf. Sci.* **1992**, *278*, 146–156.
- (17) Zhong, Q.; Vohs, J. M.; Bonnell, D. A. *Surf. Sci.* **1992**, *274*, 35.
- (18) Nörenberg, H.; Tanner, R. E.; Schierbaum, K. D.; Fischer, S.; Briggs, G. A. D. *Surf. Sci.* **1998**, *396*, 52–60.
- (19) Li, M.; Hebenstreit, W.; Diebold, U. *Phys. Rev. B* **2000**, *61*, 4926.
- (20) Li, M.; Hebenstreit, W.; Diebold, U. *Surf. Sci.* **1998**, *L414*, L951–L959.
- (21) Li, M.; Hebenstreit, W.; Gross, L.; Diebold, U.; Henderson, M. A.; Jennison, R. D.; Schultz, P. A.; Sears, M. P. *Surf. Sci.* **1999**, *437*, 173–190.
- (22) Li, M.; Hebenstreit, W.; Diebold, U.; Henderson, M. A.; Jennison, D. R. *Faraday Discuss.* **1999**, *114*, 245.
- (23) Zhang, L. P.; Li, M.; Diebold, U. *Surf. Sci.* **1998**, *412/413*, 242–251.
- (24) Anderson, P. O.; Kolberg, E. L.; Jelensky, A. *Phys. Rev.* **1973**, *28*, 4956.
- (25) Bursill, L. A.; Blanchin, M. G.; Smith, D. J. *Proc. R. Soc. London, A* **1984**, *391*, 351 and 373.
- (26) Cox, P. A. *Transition Metal Oxides: An Introduction to their Electronic Structure and Properties*; Oxford University Press: New York, 1992.
- (27) Diebold, U.; Lehman, J.; Mahmoud, T.; Kuhn, M.; Leonardelli, G.; Hebenstreit, W.; Schmid, M.; Varga, P. *Surf. Sci.* **1998**, *411*, 137–153.
- (28) Somorjai, G. A. *Principles of Surface Chemistry*; Prentice-Hall: Englewood Cliffs, New Jersey, 1972.
- (29) Bennett, R. A.; Poulston, S.; Stone, P.; Bowker, M. *Phys. Rev. B* **1999**, *59*, 10341–10346.
- (30) Silsbee, R. H. *Phys. Rev. A* **1965**, *180*, 138.
- (31) Becker, J. H.; Hosler, W. R. *Phys. Rev.* **1965**, *137*, A1872–A1877.
- (32) Acket, G. A.; Volger, J. *Physica* **1966**, *32*, 1680–1692.
- (33) Smith, D. J.; Bursill, L. A.; Blanchin, M. G. *Philos. Mag. A* **1984**, *50*, 473–485.
- (34) Henderson, M. A. *Surf. Sci.* **1999**, *419*, 174.
- (35) Kunkel, R.; Poelsema, B.; Verheij, L. K.; Comsa, G. *Phys. Rev. Lett.* **1990**, *65*, 733–736.
- (36) Ernst, H.-J.; Fabre, F.; Folkerts, R.; Lapujoulade, J. J. *Vac. Sci. Technol. A* **1994**, *12*, 1809–1817.
- (37) Li, M.; Hebenstreit, W.; Diebold, U.; Henderson, M. A., unpublished.
- (38) Huntington, H. B.; Sullivan, G. A. *Phys. Rev. Lett.* **1965**, *14*, 177–178.
- (39) Sasaki, J.; Peterson, N. L.; Hoshino, K. *J. Phys. Chem. Solids* **1985**, *46*, 1267–1283.
- (40) Arita, M.; Hosoya, M.; Kobayashi, M.; Someno, M. *J. Am. Ceram. Soc.* **1979**, *62*, 443.
- (41) Derry, D. J.; Lees, D. G.; Calvert, J. M. *J. Phys. Chem. Solids* **1981**, *42*, 57.
- (42) Neild, D. J.; Wise, P. J.; Barnes, D. G. *J. Phys. D* **1972**, *5*, 2292.
- (43) Fischer, S.; Munz, A. W.; Schierbaum, K.-D.; Göpel, W. *Surf. Sci.* **1995**, *337*, 17–30.
- (44) Diebold, U.; Anderson, J. F.; Ng, K.-O.; Vanderbilt, D. *Phys. Rev. Lett.* **1996**, *77*, 1322.